Orienting the charge transfer path of type-II heterojunction for photocatalytic hydrogen evolution

Hairui Cai[a], Bin Wang[a,*], Laifei Xiong[a], Jinglei Bi[a], Longyun Yuan[a], Guidong Yang[b], Shengchun Yang[a,c,*]

[a] School of Science, MOE Key Laboratory for Non-equilibrium Synthesis and Modulation of Condensed Matter, State Key Laboratory for Mechanical Behavior of Materials, Xi'an Jiaotong University, Xi'an, 710049, China
[b] XJTU-Oxford Joint International Research Laboratory of Catalysis, School of Chemical Engineering and Technology, Xi'an Jiaotong University, Xi'an, Shaanxi, 710049, China
[c] Collaborative Innovation Center of Suzhou Nano Science and Technology, Suzhou Academy of Xi'an Jiaotong University, 215000, Suzhou, China

ARTICLE INFO

ABSTRACT

One of the bottlenecks for photocatalytic H$_2$ generation is the severe recombination of photoexcited charge carriers in photocatalysts. As an effective approach, constructing heterojunction with type II band alignment has been applied for efficient charge separation in photocatalysts during the photocatalytic process. By compositing g-C$_3$N$_4$ and P25 as a model photocatalyst, the limited charge separation efficiency and random charge transfer paths are discovered in this conventional type II heterostructured g-C$_3$N$_4$/P25. In order to overcome these shortcomings in g-C$_3$N$_4$/P25, we designed a type II heterostructured photocatalyst with oriented transfer path for photo-excited charges during the real photocatalysis process via a one-pot synthesis strategy, in which the separation efficiency was much improved. The as-prepared g-C$_3$N$_4$/P25(N)-Pd photocatalyst exhibits a tremendously enhanced photocatalytic activity, which is 8.7 and 24.5 times that of g-C$_3$N$_4$ under visible light and full wave light irradiation, respectively.

1. Introduction

The utilization of solar energy can not only meet the energy demands in the future, but also overcome the environmental pollution caused by the fossil fuels [1,2]. Semiconductor-based photocatalysis for photocatalytic H$_2$ generation can convert solar energy directly to hydrogen energy, having attracted tremendous interests from scientists since the pioneer work by Fujishima and Honda in 1972 [3–6]. During the photocatalytic process, the photo-generated charge carriers are separated and transferred to the active sites for the surface redox reactions. At the same time, the recombination of photo-excited holes and electrons (h-e), which is a competition for charge separation, occurs both inside and surface of semiconductors, thus greatly limiting their photocatalytic performance in practical application [7,8]. Therefore, it is an urgent issue to design a photocatalytic system with high efficiency of charge separation and transmission.

In order to suppress the h-e recombination, various strategies have been applied to promote the charge separation, such as constructing heterojunction [6,9–14] or homojunction [15–18], tailoring the

morphology or crystal facets of photocatalysts for promotion of spatially photo-induced charge separation [19–31], regulating their electronic structure by introducing heteroatoms [32–34]. Among them, compositing different semiconductor by forming heterojunction with type II band alignment structure has been demonstrated as a powerful approach to efficiently separate the photo-generated electron-hole pairs for photocatalytic reaction [13,35–39]. For example, Wang et al. reported that constructing the heterojunction between ultra-thin g-C$_3$N$_4$ nanosheets and TiO$_2$ nanotubes could effectively reduce the photo-induced charge recombination so as to improve their photocatalytic performance [40]. Zhang and coworkers synthesized the van der Waals (vdW) type II heterostructures that consisted of ZrS$_2$ nanosheets and metal-free 2-dimensional (2D) sustainable materials with tunable band structure. The as-prepared vdW heterostructured 2D photocatalyst showed promising visible-light response and excellent charge carriers separation efficiency [41]. Yu presented a type-II heterostructured polymer by copolymerizing N-annulated donor into the g-C$_3$N$_4$ skeleton. Such novel heterojunction not only extended the visible-light response range but also promoted the photoexciton separation within

polymer/g-C$_3$N$_4$ [42]. Besides, Aziz Habibi-Yangjeh reported that constructing g-C$_3$N$_4$/Fe$_2$O$_3$ and g-C$_3$N$_4$/AgCl heterojunction can improve separation of carriers [43–45].

The theoretical studies have proved that the photo-excited electrons would transfer across the type II heterojunction from the conduction band (CB) of one semiconductor (A) to that of the other semiconductor (B) with less negative conduction band bottom, while the photo-excited holes transfer from the valence band (VB) of semiconductor B to that of A during the photocatalysis process, thus effectively separating the photo-generated charge carriers in the heterostructured composite [9] Hence, it is indeed a useful strategy to design a heterojunction with type II band alignment for efficient photocatalysis. However, there are still some issues that we usually ignore in the conventional type II heterojunction in the real photocatalytic process. For example, are all photo-excited charge carriers separated by the type II heterojunction? If not, how to boost the separation efficiency of charge carriers in the real photocatalysis process?

In this work, two kinds of composites, which mainly consisted of g-C$_3$N$_4$ and P25, with type II band alignment heterojunction were synthesized. We found the limited charge separation and random charge transfer paths in conventional heterostructured photocatalyst (g-C$_3$N$_4$/P25), thus leading to a relatively low photocatalytic performance. In order to further improve its separation efficiency, we designed a type II heterostructured photocatalyst (g-C$_3$N$_4$/P25(N)-Pd) with oriented transfer path for photo-excited charges during the photocatalysis process via a one-pot synthesis strategy. Under visible light and full-wave light irradiation, the as-prepared photocatalyst g-C$_3$N$_4$/P25(N)-Pd exhibited a tremendously enhanced photocatalytic activity, which was 4.6 and 9.5 times that of conventional heterostructured composite g-C$_3$N$_4$/P25, and 8.7 and 24.5 times that of g-C$_3$N$_4$, respectively. The basic mechanism for the enhanced photocatalytic activity was systemically studied in detail.

2. Experimental section

2.1. Chemicals and materials

Urea (CO(NH$_2$)$_2$), triethanolamine ((HOCH$_2$CH$_2$)$_3$N, TEOA), iso-propanol and anhydrous sodium sulfate were purchased from Sinopharm Chemical Reagent Co., Ltd. P25 (Titanium dioxide nano-particles, NPs) were purchased from Evonik Degussa. Chloropalladic acid (H$_2$PdCl$_4$) was offered by Alfa Aesar, A Johnson Matthey Company. Nafion solution (5%) was purchased from Sigma-Aldrich Co., Ltd. All the reagents were standard analytical grade without further purification.

2.2. Preparation of P25-Pd precursors

In brief, 500 mg P25, 200 μL deionized H$_2$O and 85 μL 277 mM H$_2$PdCl$_4$ solution were added and ground in an agate mortar to form a sticky slurry, and ground by a wet-grinding process until the mixture was completely dry. The weight ratio of P25 and Pd was 1:200.

2.3. Preparation of g-C$_3$N$_4$/P25(N)-Pd and g-C$_3$N$_4$/P25 samples

Typically, 800 mg urea and 50 mg P25-Pd dry precursors (or 50 mg P25) were added in the agate mortar, then mixed and ground for 30 min. Then, the obtained light yellow precursor was put into an alumina crucible with aluminized paper cover, and calcinated in a muffle furnace at 500 °C for 3 h with a heating rate of 5 °C/min. The final products g-C$_3$N$_4$/P25(N)-Pd (or g-C$_3$N$_4$/P25) were collected for use without further treatment.

2.4. Preparation of P25(N)-Pd

A certain amount of g-C$_3$N$_4$/P25(N)-Pd was put into an alumina

crucible and calcinated in a muffle furnace at 530 °C for 5 min with a heating rate of 5 °C/min. The final obtained sample P25(N)-Pd were collected for use without further treatment.

2.5. Characterization

The transmission electron microscopy (TEM) images, high-resolution TEM (HRTEM) images, and the high angle annular dark field-scanning transmission electron microscopy (HAADF-STEM) images were obtained from a JEOL JEM-F200(HR) transmission electron microscope at an accelerating voltage of 200 kV. Elemental analysis of materials was characterized by Energy-Dispersive X-ray detector (EDX) which was mounted in the above JEOL JEM-F200(HR) transmission electron microscope. The X-ray diffraction (XRD) patterns of the as-prepared materials were obtained from a Bruker D8 ADVANCE diffractometer. X-ray photoelectron spectroscopy (XPS) measurements were conducted on a Thermo Fisher ESCALAB Xi + with monochromatic Al Kα radiation (hν =1486.69 eV), and with the pressure of sample analysis chamber under high vacuum < 5 × 10^{-10} mbar. All binding energies were referenced to the C 1s peak at 284.8 eV. UV–vis diffuse reflection spectra of the materials were measured on a UV–vis spectrophotometer (HITACHI U4100 instrument) using BaSO$_4$ as the reference. The N$_2$ adsorption-desorption isotherms experiments were performed at 77.3 K using an ASAP 2020 Micromeritics analyzer after degassing the samples at 150 °C for 8 h, and the surface area of the as-prepared materials were determined using the Brunauer-Emmett-Teller (BET) methods. Fourier transform infrared (FT-IR) spectroscopy was measured by a Bruker Vextex 70 fourier transform infrared spectrometer using the KBr pellets. The content of Pd in the real catalyst was analyzed on an Inductively Coupled Plasma Mass Spectrometer (ICP-MS) (NexIONTM 350D, PerkinElmer, USA). Thermal gravimetric analysis (TGA) was obtained on a Hitachi STA7200 Thermal Analysis System. Photoluminescence (PL) spectra was recorded at room temperature with an Edinburgh FLS9 Instrument under the excitation wavelength of 337 nm. The time-resolved fluorescence measurements were observed at 460 nm.

2.6. Photocatalytic reaction

In a typical experiment of photocatalytic H$_2$ generation, photocatalyst powder (12.5 mg) and 8 mL TEOA were dispersed into 72 mL deionized water with a resistivity of 18.25 MΩ cm by sonication for 30 min. After being purged with high-purity N$_2$ gas, the suspension was irradiated using a 300 W Xe lamp under the full-wave light and visible light (a 400 nm cutoff filter) for 4 h, respectively. During the light irradiation, the generated hydrogen gas was gathered at the given time intervals and analyzed by gas chromatography (GC) equipped with a thermal conductive detector (TCD) and high-purity N$_2$ carrier gas. Additionally, the apparent quantum yield (AQY) was measured under visible light irradiation (λ = 420 ± 10 nm), and was calculated based on the Eq. (1):

$$AQE = \frac{Ne}{Np} \times 100\%$$
(1)

where Ne is the number of reaction electrons, Np is the number of incident photons.

2.7. Preparation of working electrodes

Typically, catalyst (g-C$_3$N$_4$, g-C$_3$N$_4$/P25 or g-C$_3$N$_4$/P25(N)-Pd) was dispersed in 1 mL isopropanol with 25 μL nafion (0.5%) solution to form a suspension solution with a concentration of 5 mg/mL by sonication. Then, 5 μL catalyst solution was loaded onto the L-type glassy carbon electrode. The area of sample-coated was fixed ca. 0.25 cm^2. Finally, the working electrode was dried in a vacuum oven at room temperature for overnight.

2.8. Photoelectrochemical and electrochemical testing

Photoelectrochemical and electrochemical measurements were measured by an electrochemical workstation (CHI760 Instruments) based on a conventional three-electrode system, where a sample-coated L-type Glassy Carbon Electrode, platinum foil (2 × 2 cm) and a saturated calomel electrode (SCE) were used as the working electrode, counter electrode and reference electrode, respectively. Before the transient photocurrent response and electrochemistry impedance spectroscopy (EIS) tests began, the electrolyte solution of 0.5 M Na_2SO_4 solution containing 10 vol % TEOA was purged with N_2 gas for 30 min. The frequency range of EIS measurement was tested at -1.0 V vs. SCE from 0.1 Hz to 10^6 Hz, and the amplitude was 5 mV. Transient photocurrent responses were measured at 1.5 V vs SCE. A 300 W xenon lamp coupled with a 400 nm cutoff filter was used as the light source.

3. Results and discussion

The designed heterostructured g-C_3N_4/P25(N)-Pd composite was synthesized by using a one-pot method. As described in the Experimental Section and Scheme S1, a certain amount of H_2PdCl_4 solution and P25 were ground until the mixture was completely dry, making the H_2PdCl_4 molecules being absorbed on the surface of P25. Then, the obtained dry powder mixed with urea, and finally calcinated at 500 °C to obtain the designed g-C_3N_4/P25(N)-Pd heterojunction. For comparison, the conventional g-C_3N_4/P25 composite was synthesized by directly calcining the mixture of P25 and urea, as reported in Wang's work [40]. Figure S1a displays the XRD patterns of the g-C_3N_4, P25, g-C_3N_4/P25 and g-C_3N_4/P25(N)-Pd. Both of g-C_3N_4/P25 and g-C_3N_4/P25(N)-Pd show the diffraction peaks for P25, and no obvious peaks for g-C_3N_4 due to the higher crystalline of P25 than that of g-C_3N_4. FT-IR spectra of the conventional g-C_3N_4/P25 and the designed heterostructured g-C_3N_4/P25(N)-Pd show the characteristic peaks of g-C_3N_4 and P25, proving the existence of g-C_3N_4 and P25 in both of these two samples (Figure S1b). The surface elemental composition and chemical states of g-C_3N_4/P25 and g-C_3N_4/P25(N)-Pd were further measured by XPS, as shown in Figure S2. For both of g-C_3N_4/P25 and g-C_3N_4/P25(N)-Pd, all of O 1s, N 1s and C 1s peaks are observed (Figure S2a), and the tri-s-triazine structure of g-C_3N_4 is preserved in these two samples (Figure S2b) [46]. When compared with g-C_3N_4, the peak shift of C−N═C to higher binding energies in N1 s spectra (Figure S2c) of g-C_3N_4/P25 and g-C_3N_4/P25(N)-Pd suggest the formation of interface between g-C_3N_4 and P25 in both these two samples [40]. The Ti $2p_{3/2}$ and Ti $2p_{1/2}$ peaks of g-C_3N_4/P25 do not show any obvious shift in contrast to those of P25, revealing the similar chemical environment of Ti atoms in g-C_3N_4/P25 with that in P25, and no N atoms are doped into P25 of g-C_3N_4/P25. While these two peaks for g-C_3N_4/P25(N)-Pd shift to lower binding energy, indicating that N atoms are introduced into the lattice of P25 during the thermal treatment (Figure S2d), in consistent with previous reports [47,48]. In order to further confirm the N was doped into P25, a combination of TG and XPS characterization was performed. As shown in Figure S3, the g-C_3N_4 in the sample of g-C_3N_4/P25(N)-Pd can be completely decomposed when the temperature was above 530 °C, thus obtaining the remained P25(N)-Pd. And the following XPS spectrum of the P25(N)-Pd sample clearly shows the signal that is resulted from the N 1s (Figure S4), indicating that the N was really doped into P25 in g-C_3N_4/P25(N)-Pd during the calcinating process.

Fig. 1 shows the UV–vis absorption spectra and XPS valence band spectra of g-C_3N_4, P25(N)-Pd, P25, and g-C_3N_4/P25(N)-Pd. It is clear that the absorption edge for pure g-C_3N_4 and P25 are around 450 nm and 390 nm, respectively, and the absorption edge of P25(N)-Pd is about 420 nm, which is between that of C_3N_4 and P25. The g-C_3N_4/P25(N)-Pd heterojunction shows a similar absorption edge like g-C_3N_4. Based on the Kubellka-Munk method [49], the band gap for g-C_3N_4, P25, and P25(N)-Pd are estimated to be ca. 2.76 eV, 3.2 eV, and

2.95 eV, respectively(Fig. 1b). By using valence band XPS spectra, the valence band maximum (VBM) edge potentials of g-C_3N_4, P25, and P25(N)-Pd are measured to be ~2.25 eV, ~2.75 eV and ~2.5 eV, respectively (Fig. 1c). Combined with the results of UV–vis spectra and valence band XPS spectra, the conduction band edge potentials of g-C_3N_4, P25, and P25(N)-Pd are estimated to be -0.51 eV, -0.45 eV and -0.45 eV, respectively. Therefore, we can confirm that both of g-C_3N_4/P25 and g-C_3N_4/P25(N)-Pd possess the type II band alignment structure, as shown in Fig. 1d.

Figs. 2a-b show the TEM images of the as-prepared g-C_3N_4/P25(N)-Pd composite. The NPs with high contrast are P25, while the lamellar nanosheets with low contrast are g-C_3N_4. Fig. 2c shows the HRTEM image of the sample, from which the Pd NPs can be observed on the surface of P25. The interplanar space of 0.35 and 0.20 nm shown in Figs. 2d correspond to the (101) plane of the TiO_2 anatase phase and (100) plane of Pd NPs, respectively, confirming the Pd NPs being well loaded on the surface of P25 in g-C_3N_4/P25(N)-Pd. The EDS line scan in Fig. 2f was recorded from the HAADF-STEM image of g-C_3N_4/P25(N)-Pd in Fig. 2e (the

green line OO'). The C Kα, N Kα, O Kα, Pd Lα, and Ti Kα signals are detected and recorded in the line scan profile (Fig. 2f). Especially, the signal resulting from Pd only appears in the regions of Ti signal (inset in Fig. 2f), indicating that Pd NPs are mainly deposited on the surface of P25. The relatively weak signal intensity of Pd element in contrast to that of C, N, Ti, O elements reveals the low Pd content (0.5%, measured by ICP). The EDS spectra in Fig. 2g further confirms the existence of Pd in the sample, which is consistent with the results of line scan profile in Fig. 2f. Based on the above analysis, we inferred that Pd NPs were mainly deposited on the surface of P25 in heterostructured g-C_3N_4/P25(N)-Pd, and the diagram of g-C_3N_4/P25(N)-Pd is presented in Fig. 2h.

Although it has been widely accepted that the photoexcited charge carriers can be effectively separated by the heterojunction of g-C_3N_4 and P25 [40,46], whether all the photo-induced charge carriers can be separated by the type II heterojunction in g-C_3N_4/P25 is still uncertain. Therefore, an in-situ photo-deposition experiment for loading Pd NPs on g-C_3N_4/P25 catalysts was performed. In brief, the conventional heterostructured g-C_3N_4/P25 was dispersed in a 10 vol% TEOA solution containing H_2PdCl_4 and then the Pd could be loaded by the in-situ photo-deposition process. Theoretically, under the light irradiation, the photo-induced electrons from g-C_3N_4 would be transferred to P25 across the heterojunction between g-C_3N_4 and P25. If all electrons were transferred to P25, the Pd^{2+} would be reduced by the photo-generated electrons to form Pd NPs on the surface of P25. Otherwise, the Pd nanoparticles would be in-situ photo-deposited on the surface of both P25 and g-C_3N_4. Figure S5a shows the TEM image of the Pd loaded g-C_3N_4/P25 after the photo-deposition experiment, and the morphology of the sample is similar with that of g-C_3N_4/P25(N)-Pd. Figures S5b and S5c are recorded from the red and blue dashed rectangle areas in Figure S5a, respectively, from which one can see that the Pd NPs are deposited both on the surface of g-C_3N_4 nanosheets and P25. Figure S5d shows the HAADF-STEM image, in which the lamellar g-C_3N_4 nanosheets with low contrast, P25 NPs (ca. 50 nm) with medium contrast and Pd NPs (ca. 5 nm) with high contrast can be well recognized (indicated by white arrows). Elemental mapping (Figures S5e-i) show the C, N, Ti, O and Pd elements distribution in Figure S5d. Furthermore, the overlay of N, Ti and Pd elements (Figs. 5j) also confirms that Pd NPs are deposited on the surface of both g-C_3N_4 and P25. Thus, the illustration of Pd loaded conventional heterostructured g-C_3N_4/P25 by in-situ photo-deposition method is proposed, as shown in Figure S5l. It implies that only part of the photo-excited electron-hole pair can be separated by the type II heterojunction in g-C_3N_4/P25 and the charge transfer path are random in such conventional heterostructured g-C_3N_4/P25.

Different from the conventional g-C_3N_4/P25 photocatalyst loaded with Pd NPs by in-situ photo-deposition method, in our designed type II heterostructured g-C_3N_4/P25(N)-Pd, the Pd NPs only deposited on the
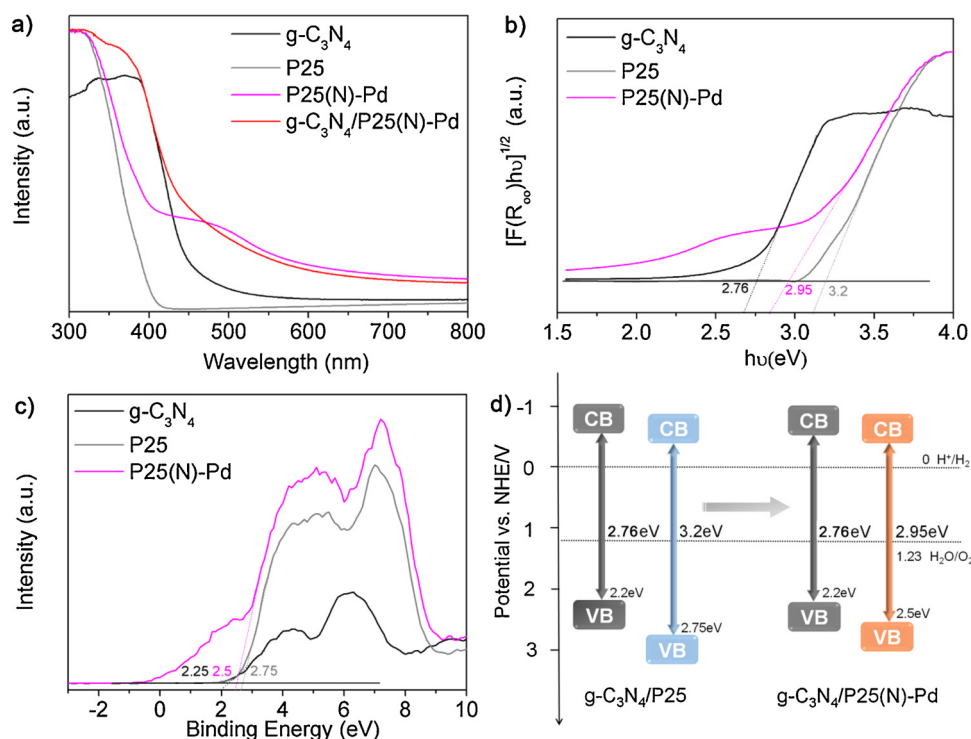
Fig. 1. a) The UV–vis absorption spectra of g-C_3N_4, P25, P25(N)-Pd and g-C_3N_4/P25(N)-Pd; b) The plots of transformed K-M function [F$(R_\infty)h\nu]^{1/2}$ vs. hν for g-C_3N_4, P25 and P25(N)-Pd; c) XPS valence band spectra of g-C_3N_4, P25 and P25(N)-Pd; d) The illustration of band structures for g-C_3N_4/P25 and g-C_3N_4/P25(N)-Pd, respectively.

surface of P25. Thus, we suppose that the photo-excited electrons will be transferred from the CB of g-C_3N_4 to that of P25, then rapidly immigrated to the Pd NPs on P25. Consequently, the transferred electrons from g-C_3N_4 to P25 can rapidly participate in the photocatalytic reaction on the surface of Pd NPs for H_2 evolution, resulting in enhanced charge separation efficiency of g-C_3N_4/P25(N)-Pd heterojunction in contrast to that of conventional g-C_3N_4/P25 with random charge transfer path. In order to verify the proposed mechanism of the designed g-C_3N_4/P25(N)-Pd, a series of photocatalytic experiments were performed under visible light ($\lambda > 400$ nm) and full wave irradiation, respectively. As shown in Fig. 3a, after loading the same amount of Pd (0.5 wt %) by in-situ photo-deposition method, pure g-C_3N_4 exhibits a relatively lower average rate of H_2 evolution of ~0.123 mmol h^{-1} g^{-1} under visible light irradiation. While the conventional heterostructured g-C_3N_4/P25 shows a higher H_2-generation rate of 0.231 mmol h^{-1} g^{-1} than that of pure g-C_3N_4. Surprisingly, the designed g-C_3N_4/P25(N)-Pd presents the highest hydrogen evolution rates of ~1.07 mmol h^{-1} g^{-1}, which is 8.7 and 4.6 times of that g-C_3N_4 and g-C_3N_4/P25, respectively. Moreover, under full wave irradiation, the photocatalytic hydrogen production activity of g-C_3N_4/P25(N)-Pd is up to 6.33 mmol h^{-1} g^{-1}, which is 24.5 and 9.5 times that of pure g-C_3N_4 (~0.258 mmol h^{-1} g^{-1}) and g-C_3N_4/P25 (~0.664 mmol h^{-1} g^{-1}), respectively (Fig. 3b). In addition, the BET surface areas for g-C_3N_4, g-C_3N_4/P25, g-C_3N_4/P25(N)-Pd were estimated to be 61.3 m^2 g^{-1}, 61.8 m^2 g^{-1} and 75.8 m^2 g^{-1}, respectively (Table S1, Figure S6). Therefore, the photocatalytic activities over g-C_3N_4, g-C_3N_4/P25, g-C_3N_4/P25(N)-Pd were normalized with respect to their BET surface areas and obtained under visible light irradiation (Fig. 3c) and full wave irradiation (Fig. 3d). Obviously, the time-coursed photocatalytic H_2 evolution that are normalized to specific surface area over these three samples are in the same activity order, demonstrating the superiority of the designed type II heterojunction g-C_3N_4/P25(N)-Pd. Moreover, the hydrogen evolution rate (HER) of g-C_3N_4/P25(N)-Pd are much higher than that of g-C_3N_4 and P25(N)-Pd, even than the sum of HER of these two samples, under both visible light irradiation and full-wave light irradiation (Table S2), respectively, confirming that the photocatalytic performance enhancement of g-C_3N_4/P25(N)-Pd indeed resulted from the designed type II heterojunction with targeted charge transfer path. We conducted a

series of experiments to obtain the AQY of the 0.5 wt% Pd loaded g-C_3N_4, 0.5 wt% Pd loaded g-C_3N_4/P25 and g-C3N4/P25(N)-Pd under the 420 nm light irradiation. The AQY of g-C_3N_4/P25(N)-Pd can reach up to 3.98%, which is higher than those of 0.5 wt% Pd loaded g-C_3N_4 (1.36%) and 0.5 wt% Pd loaded g-C_3N_4/P25 (1.51%), respectively. As shown in Figure S7, cycle experiments of the photocatalytic H_2 generation are carried out to confirm the photocatalytic H_2 evolution stability of g-C_3N_4/P25(N)-Pd. The hydrogen evolution activity of g-C_3N_4/P25(N)-Pd was maintained without noticeable leveling off tendency of photocatalytic performance in consecutive 16 h irradiation runs, revealing good persistence of g-C_3N_4/P25(N)-Pd photocatalyst. In order to further prove the good stability of this photocatalyst, a series of related characterizations (XRD, FT-IR, XPS and SEM) of g-C_3N_4/P25(N)-Pd after photocatalytic tests are carried out. Obviously, after the photocatalytic H_2 generation test, both of P25 and g-C_3N_4 in g-C_3N_4/P25(N)-Pd are stably preserved (Figure S8). Meanwhile, the g-C_3N_4/P25(N)-Pd photocatalyst before and after photocatalytic test exhibit no obvious morphology changes (Figure S9). All these results indicate that the g-C_3N_4/P25(N)-Pd possesses the remarkable stability. Additionally, the rate of photocatalytic H_2 evolution over g-C_3N_4 based photocatalysts with type II heterojunction published in recent year are summarized in Table 1. It is clear that the g-C_3N_4/P25(N)-Pd shows higher activity when compared with the reported g-C_3N_4/TiO$_2$-based photocatalysts, further confirming that the oriented charge transfer path in our designed type II heterojunction contributes much to its photocatalytic performance.

EIS characterization is a powerful tool to explore the charge-transfer resistances in the electrodes and at the interface of electrode and electrolyte. Fig. 4a shows the EIS Nynquist plots of g-C_3N_4, g-C_3N_4/P25 and g-C_3N_4/P25(N)-Pd, respectively, and such results are further fitted to an equivalent circuit (the inset of Fig. 4a). Obviously, the g-C_3N_4/P25(N)-Pd possesses the lowest R_{ct} value (168 Ω) when compared with that of g-C_3N_4/P25 (236 Ω) and g-C_3N_4 (318 Ω) due to the smallest arc radius of g-C_3N_4/P25(N)-Pd. Such result indicates that the charge carrier transfer and separation on g-C_3N_4/P25(N)-Pd are much enhanced, thus leading to an improved photocatalytic activity [40]. The transient photocurrent density of g-C_3N_4/P25(N)-Pd was ca. 2.5 times that of g-C_3N_4/P25 (Fig. 4b), suggesting the promoted separation of photo-induced charge carriers at the interfaces between g-C_3N_4 and P25(N)-
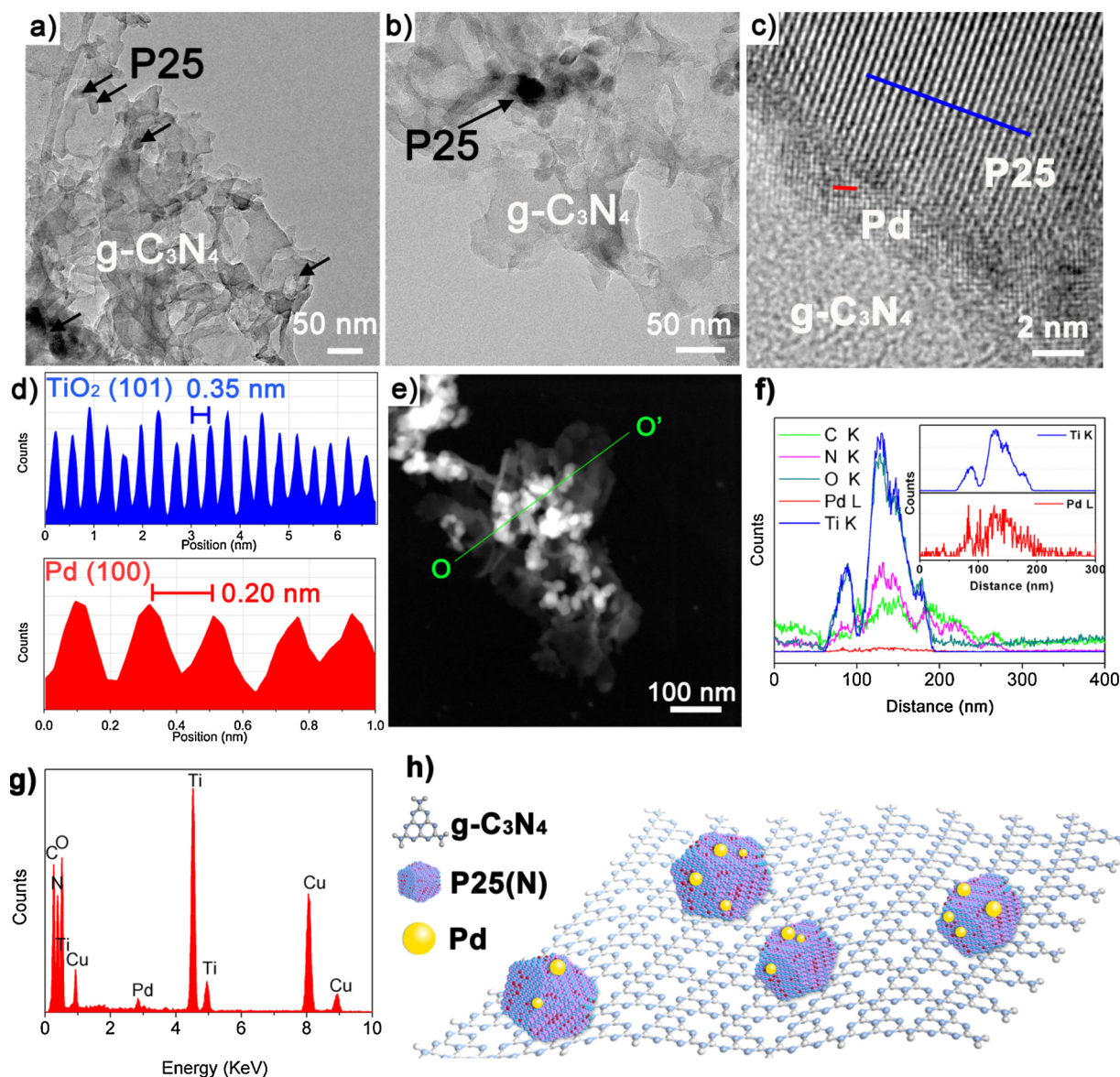
Fig. 2. a) TEM image of g-C$_3$N$_4$/P25(N)-Pd; b) enlarged TEM images recorded from different region of g-C$_3$N$_4$/P25(N)-Pd; c) HRTEM image of g-C$_3$N$_4$/P25(N)-Pd; line analyses of d) TiO$_2$ and Pd, respectively, and the corresponding analysis region and orientation were marked in c) for TiO$_2$ (blue line) and Pd (red line), respectively; e) HAADF-STEM image of g-C$_3$N$_4$/P25(N)-Pd; f) EDX line scan of C Kα, N Kα, O Kα, Pd Lα and Ti Kα signal recorded from the green line OO' in e); g) The EDX spectra obtained from g-C$_3$N$_4$/P25(N)-Pd in e). h) The diagram of type II heterostructured g-C$_3$N$_4$/P25(N)-Pd (For interpretation of the references to colour in this figure legend, the reader is referred to the web version of this article.).

Pd. We also study the PL spectra for these three samples to investigate their charge separation efficiency, as shown in Fig. 4c. The PL intensity over g-C$_3$N$_4$/P25 is much lower than that of pure g-C$_3$N$_4$, revealing that the conventional heterojunction between g-C$_3$N$_4$ and P25 can effectively suppress the charge recombination in g-C$_3$N$_4$/P25. The lowest PL intensity for g-C$_3$N$_4$/P25(N)-Pd indicates that the designed type II heterojunction with targeted charge transfer path can more effectively separate and transfer the photo-induced charge carriers in contrast to conventional g-C$_3$N$_4$/P25 heterojunction. The limited charge separation of conventional g-C$_3$N$_4$/P25 heterojunction may be due to the accumulation of electrons, which are transferred from g-C$_3$N$_4$, on P25 hindering the charge separation on the heterojunction between g-C$_3$N$_4$ and P25. Fig. 4d displays the time-resolved PL emission decay spectra over g-C$_3$N$_4$, g-C$_3$N$_4$/P25 and g-C$_3$N$_4$/P25(N)-Pd, respectively. The g-C$_3$N$_4$/P25 exhibits a shorter average exciton lifetime of 12.30 ns (Table S3) than that of g-C$_3$N$_4$ (22.01 ns, Table S3), indicating the enhanced charge separation by conventional type II heterojunction in g-C$_3$N$_4$/

P25. The decreased average exciton lifetime from 12.30 ns for g-C$_3$N$_4$/P25 to 8.50 ns (Table S3) for g-C$_3$N$_4$/P25(N)-Pd reveals that the photoexciton dissociation is accelerated in g-C$_3$N$_4$/P25(N)-Pd in contrast to g-C$_3$N$_4$/P25, confirming that the designed type II heterojunction with targeted charge transfer path further improves the separation efficiency of charge carriers [62,63].

Based on the above experimental results and analysis, the plausible photocatalytic mechanisms for these three samples are proposed in Fig. 5. Briefly, under the light irradiation, there is severe recombination of photoinduced electrons and holes in g-C$_3$N$_4$ (Fig. 5, left), resulting in its poor photocatalytic performance. In the conventional composite g-C$_3$N$_4$/P25, the heterojunction between g-C$_3$N$_4$ and P25 can separate the electrons and holes efficiently. However, as evidenced by our experiment, two charge transfer paths (Fig. 5, middle, Path I and Path II) exist, thus resulting in the random transfer for photoexcited electrons and leading to the limited charge separation. While in the designed g-C$_3$N$_4$/P25(N)-Pd heterojunctions, the targeted charge transfer path is
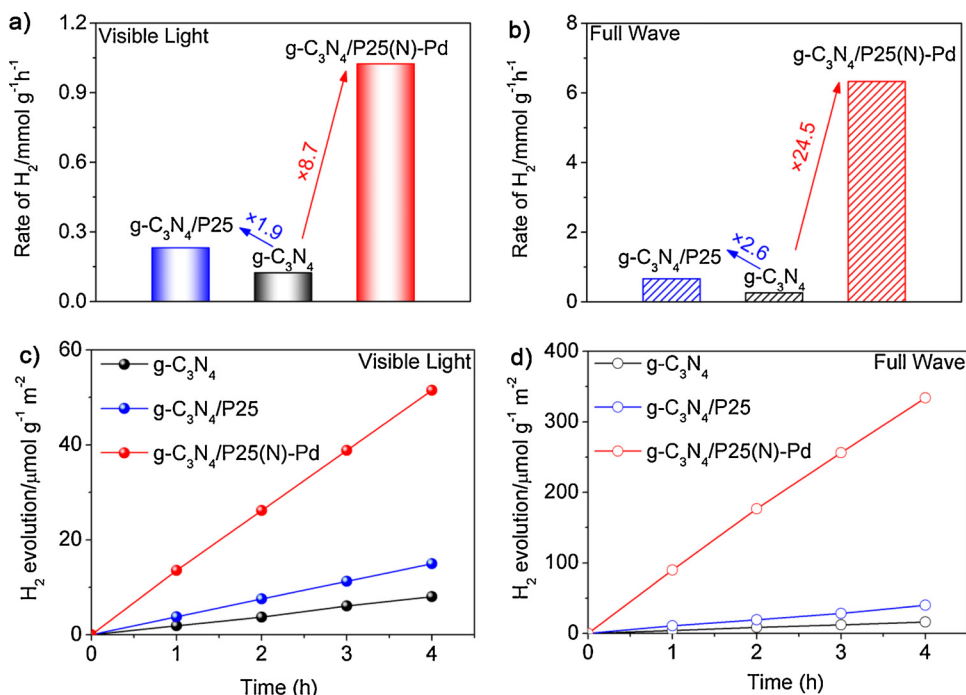
Fig. 3. Rates of photocatalytic hydrogen production over 0.5 wt% Pd loaded g-C$_3$N$_4$, 0.5 wt% Pd loaded g-C$_3$N$_4$/P25 and g-C$_3$N$_4$/P25(N)-Pd under a) visible light ($\lambda > 400$ nm) irradiation and b) full-wave irradiation, respectively. Time-coursed photocatalytic activities normalized to specific BET surface area over 0.5 wt% Pd loaded g-C$_3$N$_4$, 0.5 wt% Pd loaded g-C$_3$N$_4$/P25 and g-C$_3$N$_4$/P25(N)-Pd under c) visible light irradiation ($\lambda > 400$ nm) and d) full-wave irradiation, respectively.

Table 1
Summary of g-C$_3$N$_4$ based photocatalysts in terms of HER rate.

Photocatalysts	Co-catalyst	Mass Ratio (wt%)	Rates of H$_2$ Production (mmol h^{-1} g^{-1})	Light Source	Ref.
g-C$_3$N$_4$/P25(N)-Pd	**Pd**	**0.5**	**1.07**	**$\lambda > 400$ nm**	**Our work**
g-C$_3$N$_4$/P25(N)-Pd	**Pd**	**0.5**	**6.33**	**Full wave**	**Our work**
g-C$_3$N$_4$/TiO$_2$ hierarchical spheres	Pt	0.5	0.329	$\lambda > 420$ nm	[50]
brookite-TiO$_2$/g-C$_3$N$_4$	Pt	1	0.353	$\lambda > 400$ nm	[51]
g-C$_3$N$_4$/TiO$_2$	Pt	3	0.513	$\lambda > 420$ nm	[52]
O-g-C$_3$N$_4$/TiO$_2$	Pt	3	0.587	$\lambda > 400$ nm	[53]
CoTiO$_3$/g-C$_3$N$_4$	Pt	3	0.858	$\lambda > 420$ nm	[54]
g-C$_3$N$_4$/SrTiO$_3$	Pt	3	0.967	$\lambda > 420$ nm	[55]
WO$_3$/g-C$_3$N$_4$	Pt	2	0.982	Full wave	[56]
C-TiO$_2$/g-C$_3$N$_4$	Pt	3	1.15	$\lambda > 420$ nm	[57]
porous g-C$_3$N$_4$/TiO$_2$ nanotubes	Pt	3	1.36	$\lambda > 400$ nm	[40]
TiO$_2$/C$_3$N$_4$	Pt	1	1.54	Full wave	[58]
g-C$_3$N$_4$/TiO$_2$ yolk–shell spheres	×	×	0.112	$\lambda > 420$ nm	[59]
g-C$_3$N$_4$/TiO$_2$Mesocrystals	×	×	0.144	$\lambda > 420$ nm	[60]
g-C$_3$N$_4$@TiO$_2$	×	×	0.446	$\lambda > 420$ nm	[61]

designed. First, the photo-excited charge carriers in g-C$_3$N$_4$ are efficiently separated by the heterojunction between g-C$_3$N$_4$ and P25(N). Then, the electrons, which are transferred from the CB of g-C$_3$N$_4$ directionally to the CB of P25(N), can rapidly migrate to the Pd NPs that are in-site anchored on the surface of P25(N). Consequently, the transferred electrons from g-C$_3$N$_4$ to P25 can rapidly participate in the photocatalytic reaction for H$_2$ evolution (Fig. 5, right), leading to the more effective charge separation in contrast to that of g-C$_3$N$_4$/P25.

photocatalytic hydrogen evolution activity than that of conventional heterostructured g-C$_3$N$_4$/P25 under both visible light and full-wave light irradiation. Moreover, the photocatalytic activity of the designed photocatalyst is 8.7 and 24.5 times that of g-C$_3$N$_4$ under visible light and full-wave light irradiation, respectively. This work sheds a light on the charge transfer mechanism in conventional type II heterostructured photocatalyst and provides a methodology for promoting the charge separation in such heterostructured photocatalyst with type II band alignment.

4. Conclusions

In summary, we found the limited charge separation and random charge transfer paths in the conventional heterostructured photocatalyst with type II band alignment, and developed a one-pot approach to synthesize a novel type II heterostructured photocatalyst with targeted charge transfer path for enhanced charge separation efficiency. In our designed photocatalyst, the photo-generated electrons and holes can be effectively separated by the heterojunction between g-C$_3$N$_4$ and P25(N), and the electrons are then directionally transferred to the Pd NPs on the surface of P25(N) to rapidly take part in the H$_2$ evolution reaction. Therefore, the designed photocatalyst shows much higher

Fig. 4. a) EIS of g-C$_3$N$_4$, g-C$_3$N$_4$/P25 and g-C$_3$N$_4$/P25(N)-Pd in 0.5 M Na$_2$SO$_4$ solution containing 10 vol% TEOA at -1.0 V vs. SCE; b) Transient photocurrent response for g-C$_3$N$_4$/P25 and g-C$_3$N$_4$/P25(N)-Pd in 0.5 M Na$_2$SO$_4$ solution containing 10 vol% TEOA at 1.5 V vs. SCE under visible light irradiation; c) PL spectra for g-C$_3$N$_4$, g-C$_3$N$_4$/P25 and g-C$_3$N$_4$/P25(N)-Pd; d) Time-resolved PL emission decay spectra for g-C$_3$N$_4$, g-C$_3$N$_4$/P25 and g-C$_3$N$_4$/P25(N)-Pd, respectively. The inset in a) gives the corresponding equivalent circuits for these three samples, R$_s$ is the series resistance, including the electrolyte solution resistance, the sheet resistance of glassy carbon electrode and the contact resistance; R$_{ct}$ is the resistance for electron transfer, and CPE is the double-layer capacitance at the solution contact interface.
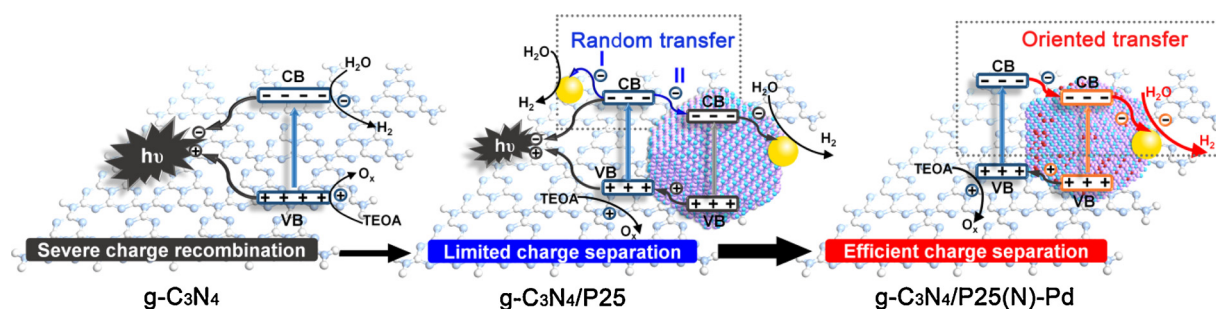

Fig. 5. Plausible mechanisms photocatalytic hydrogen evolution over g-C$_3$N$_4$, g-C$_3$N$_4$/P25, and g-C$_3$N$_4$/P25(N)-Pd, respectively. Briefly, the charge recombination in g-C$_3$N$_4$ was very severe (left); constructing g-C$_3$N$_4$/P25 can suppress the charge recombination, but the separation of charge carriers was still limited due to the random transfer paths; in the designed type II heterostructured g-C$_3$N$_4$/P25(N)-Pd, the charge separation was effectively promoted due to the targeted transfer path.

Xi'an Jiaotong University.

Appendix A. Supplementary data

Supplementary material related to this article can be found, in the online version, at doi:https://doi.org/10.1016/j.apcatb.2019.117853.

References

[1] E.A. Kozlova, V.N. Parmon, Heterogeneous semiconductor photocatalysts for hydrogen production from aqueous solutions of Electron donors, Russ. Chem. Rev. 86 (2017) 870–906, https://doi.org/10.1070/rcr4739.

[2] K.C. Christoforidis, P. Fornasiero, Photocatalytic hydrogen production: a rift into the future energy supply, Chem.Cat.Chem. 9 (2017) 1523–1544, https://doi.org/10.1002/cctc.201601659.

[3] A. Fujishima, K. Honda, Electrochemical photolysis of water at a semiconductor electrode, Nature 238 (1972) 37, https://doi.org/10.1038/238037a0.

[4] M.G. Walter, E.L. Warren, J.R. McKone, S.W. Boettcher, Q. Mi, E.A. Santori, N.S. Lewis, Solar water splitting cells, Chem. Rev. 110 (2010) 6446–6473, https://doi.org/10.1021/cr1002326.

[5] I. Roger, M.A. Shipman, M.D. Symes, Earth-abundant catalysts for electrochemical and photoelectrochemical water splitting, Int. Rev. Chem. 1 (2017) 0003, https://doi.org/10.1038/s41570-016-0003.

[6] J. Liu, Y. Liu, N. Liu, Y. Han, X. Zhang, H. Huang, Y. Lifshitz, S.-T. Lee, J. Zhong, Z. Kang, Metal-free efficient photocatalyst for StableVisible water splitting via a two-electron pathway, Science 347 (2015) 970–974, https://doi.org/10.1126/science.aaa3145.

[7] J. Li, L. Cai, J. Shang, Y. Yu, L. Zhang, Giant enhancement of internal electric field boosting bulk charge separation for photocatalysis, Adv. Mater. 28 (2016) 4059–4064, https://doi.org/10.1002/adma.201600301.

[8] X. Sheng, T. Xu, X. Feng, Rational design of photoelectrodes with rapid charge transport for photoelectrochemical applications, Adv. Mater. 31 (2019) 1805132, , https://doi.org/10.1002/adma.201805132.

[9] S.J.A. Moniz, S.A. Shevlin, D.J. Martin, Z.-X. Guo, J. Tang, Visible-light driven heterojunction photocatalysts for water splitting – a critical review, Energy Environ. Sci. 8 (2015) 731–759, https://doi.org/10.1039/C4EE03271C.

[10] J. Fu, J. Yu, C. Jiang, B. Cheng, g-C$_3$N$_4$-Based heterostructured photocatalysts, Adv. Energy Mater. 8 (2018) 1701503, , https://doi.org/10.1002/aenm.201701503.

[11] X. Yu, F. Liu, J. Bi, B. Wang, S. Yang, Improving the plasmonic efficiency of the Au nanorod-semiconductor photocatalysis toward water reduction by constructing a unique hot-dog nanostructure, Nano Energy 33 (2017) 469–475, https://doi.org/10.1016/j.nanoen.2017.02.006.

[12] Q. Wang, W. Wang, L. Zhong, D. Liu, X. Cao, F. Cui, Oxygen vacancy-rich 2D/2D BiOCl-g-C$_3$N$_4$ ultrathin heterostructure nanosheets for enhanced visible-light-driven photocatalytic activity in environmental remediation, Appl. Catal. B: Environ. 220 (2018) 290–302, https://doi.org/10.1016/j.apcatb.2017.08.049.

[13] J. Low, J. Yu, M. Jaroniec, S. Wageh, A.A. Al-Ghamdi, Heterojunction photocatalysts, Adv. Mater. 29 (2017) 1601694, , https://doi.org/10.1002/adma.201601694.

[14] M. Mousavi, A. Habibi-Yangjeh, S.R. Pouran, Review on magnetically separable graphitic carbon nitride-based nanocomposites as promising visible-light-driven photocatalysts, J. Mater. Sci: Mater. Electron. 29 (2018) 1719–1747, https://doi.org/10.1007/s10854-017-8166-x.

[15] Y. Jin, D.H. Keum, S.-J. An, J. Kim, H.S. Lee, Y.H. Lee, A. Van Der, Waals homojunction: ideal p–n diode behavior in MoSe$_2$, Adv. Mater. 27 (2015) 5534–5540, https://doi.org/10.1002/adma.201502278.

[16] G. Liu, G. Zhao, W. Zhou, Y. Liu, H. Pang, H. Zhang, D. Hao, X. Meng, P. Li, T. Kako, J. Ye, In situ bond modulation of graphitic carbon nitride to construct p–n homojunctions for enhanced photocatalytic hydrogen production, Adv. Funct. Mater. 26 (2016) 6822–6829, https://doi.org/10.1002/adfm.201602779.

[17] X. Liu, A. Chen, Y. Luo, P. Lu, Y. Dai, E. Enriquez, P. Dowden, H. Xu, P.G. Kotula, A.K. Azad, D.A. Yarotski, R.P. Prasankumar, A.J. Taylor, J.D. Thompson, Q. Jia, Conducting interface in oxide homojunction: understanding of superior properties in black TiO$_2$, Nano Lett. 16 (2016) 5751–5755, https://doi.org/10.1021/acs.nanolett.6b02454.

[18] M. Liu, Y. Chen, J. Su, J. Shi, X. Wang, L. Guo, Photocatalytic hydrogen production using twinned nanocrystals and an unanchored NiS$_x$ co-catalyst, Nat. Energy 1 (2016) 16151, https://doi.org/10.1038/nenergy.2016.151.

[19] B. Wang, M. Liu, Z. Zhou, L. Guo, Surface activation of faceted photocatalyst: when metal cocatalyst determines the nature of the facets, Adv. Sci. 2 (2015) 1500153, , https://doi.org/10.1002/advs.201500153.

[20] H.G. Yang, C.H. Sun, S.Z. Qiao, J. Zou, G. Liu, S.C. Smith, H.M. Cheng, G.Q. Lu, Anatase TiO$_2$ single crystals with a large percentage of reactive facets, Nature 453 (2008) 638, https://doi.org/10.1038/nature06964.

[21] B. Wang, S. Shen, L. Guo, Surface reconstruction of facet-functionalized SrTiO$_3$ nanocrystals for photocatalytic hydrogen evolution, Chem.Cat.Chem. 8 (2016) 798–804, https://doi.org/10.1002/cctc.201501162.

[22] Y. Zheng, L. Lin, X. Ye, F. Guo, X. Wang, Helical graphitic carbon nitrides with photocatalytic and optical activities, Angew. Chem. Int. Ed. 53 (2014) 11926–11930, https://doi.org/10.1002/anie.201407319.

[23] J. Zhu, F. Fan, R. Chen, H. An, Z. Feng, C. Li, Direct imaging of highly anisotropic photogenerated charge separations on different facets of a single BiVO$_4$ photocatalyst, Angew. Chem. Int. Ed. 54 (2015) 9111–9114, https://doi.org/10.1002/anie.201504135.

[24] R. Li, H. Han, F. Zhang, D. Wang, C. Li, Highly efficient photocatalysts constructed by rational assembly of dual-cocatalysts separately on different facets of BiVO$_4$, Energy Environ. Sci. 7 (2014) 1369–1376, https://doi.org/10.1039/C3EE43304H.

[25] R. Li, F. Zhang, D. Wang, J. Yang, M. Li, J. Zhu, X. Zhou, H. Han, C. Li, Spatial Separation of Photogenerated Electrons and Holes among {010} and {110} Crystal Facets of BiVO4, Nat. Commun. 4 (2013) 1432, https://doi.org/10.1038/ncomms2401.

[26] B. Wang, S. Shen, L. Guo, SrTiO$_3$ single crystals enclosed with high-indexed {023} facets and {001} facets for photocatalytic hydrogen and oxygen evolution, Appl. Catal. B: Environ. 166-167 (2015) 320–326, https://doi.org/10.1016/j.apcatb.2014.11.032.

[27] T. Wei, Y.-N. Zhu, Z. Gu, X. An, L.-m. Liu, Y. Wu, H. Liu, J. Tang, J. Qu, Multielectric field modulation for photocatalytic oxygen evolution: enhanced charge separation by coupling oxygen vacancies with faceted heterostructures, Nano Energy 51 (2018) 764–773, https://doi.org/10.1016/j.nanoen.2018.07.018.

[28] H. Wang, Y. Sun, Y. Wu, W. Tu, S. Wu, X. Yuan, G. Zeng, Z.J. Xu, S. Li, J.W. Chew, Electrical promotion of spatially photoinduced charge separation via Interfacial-built-in quasi-alloying effect in hierarchical Zn$_2$In$_2$S$_5$/Ti$_3$C$_2$(O, OH)$_x$ hybrids toward efficient photocatalytic hydrogen evolution and environmental remediation, Appl. Catal. B: Environ. 245 (2019) 290–301, https://doi.org/10.1016/j.apcatb.2018.12.051.

[29] S. Asadzadeh-Khaneghah, A. Habibi-Yangjeh, D. Seifzadeh, Graphitic carbon nitride nanosheets coupled with carbon dots and BiOI nanoparticles: boosting visible-light-driven photocatalytic activity, J. Taiwan Inst. Chem. Eng. 87 (2018) 98–111, https://doi.org/10.1016/j.jtice.2018.03.017.

[30] S. Asadzadeh-Khaneghah, A. Habibi-Yangjeh, K. Nakata, Decoration of carbon dots over hydrogen peroxide treated graphitic carbon nitride: exceptional photocatalytic performance in removal of different contaminants under visible light, J. Photochem. Photobiol. A: Chem. 374 (2019) 161–172, https://doi.org/10.1016/j.jphotochem.2019.02.002.

[31] H. Wang, Y. Wu, X. Yuan, G. Zeng, J. Zhou, X. Wang, J.W. Chew, Clay-inspired MXene-based electrochemical devices and photo-electrocatalyst: state-of-the-art progresses and challenges, Adv. Mater. 30 (2018) 1704561, , https://doi.org/10.1002/adma.201704561.

[32] B. Wang, H. Cai, D. Zhao, M. Song, P. Guo, S. Shen, D. Li, S. Yang, Enhanced photocatalytic hydrogen evolution by partially replaced corner-site C atom with P in g-C$_3$N$_4$, Appl. Catal. B: Environ. 244 (2019) 486–493, https://doi.org/10.1016/j.apcatb.2018.10.044.

[33] J. Ran, T.Y. Ma, G. Gao, X.-W. Du, S.Z. Qiao, Porous P-doped graphitic carbon nitride nanosheets for synergistically enhanced visible-light photocatalytic H$_2$ production, Energy Environ. Sci. 8 (2015) 3708–3717, https://doi.org/10.1039/C5EE02650D.

[34] Y. Wu, H. Wang, W. Tu, S. Wu, Y. Liu, Y.Z. Tan, H. Luo, X. Yuan, J.W. Chew, Petal-like CdS nanostructures coated with exfoliated sulfur-doped carbon nitride via chemically activated chain termination for enhanced visible-light–driven photocatalytic water purification and H$_2$ generation, Appl. Catal. B: Environ. 229 (2018) 181–191, https://doi.org/10.1016/j.apcatb.2018.02.029.

[35] Y. Wang, Q. Wang, X. Zhan, F. Wang, M. Safdar, J. He, Visible light driven type II heterostructures and their enhanced photocatalysis properties: a review, Nanoscale. 5 (2013) 8326–8339, https://doi.org/10.1039/C3NR01577G.

[36] A.V. Puga, Photocatalytic production of hydrogen from biomass-derived feedstocks, Coord. Chem. Rev. 315 (2016) 1–66, https://doi.org/10.1016/j.ccr.2015.12.009.

[37] M. Shekofteh-Gohari, A. Habibi-Yangjeh, M. Abitorabi, A. Rouhi, Magnetically separable nanocomposites based on ZnO and their applications in photocatalytic processes: a review, Crit. Rev. Environ. Sci. Technol. 48 (2018) 806–857, https://doi.org/10.1080/10643389.2018.1487227.

[38] M. Pirhashemi, A. Habibi-Yangjeh, S. Rahim Pouran, Review on the criteria anticipated for the fabrication of highly efficient ZnO-based visible-light-driven photocatalysts, J. Ind. Eng. Chem. 62 (2018) 1–25, https://doi.org/10.1016/j.jiec.2018.01.012.

[39] H. Wang, Y. Wu, T. Xiao, X. Yuan, G. Zeng, W. Tu, S. Wu, H.Y. Lee, Y.Z. Tan, J.W. Chew, Formation of quasi-core-shell In$_2$S$_3$/anatase TiO$_2$@metallic Ti$_3$C$_2$Tx hybrids with favorable charge transfer channels for excellent visible-light-photocatalytic performance, Appl. Catal. B: Environ. 233 (2018) 213–225, https://doi.org/10.1016/j.apcatb.2018.04.012.

[40] Y. Wang, X. Liu, C. Zheng, Y. Li, S. Jia, Z. Li, Y. Zhao, Tailoring TiO$_2$ nanotube-interlaced graphite carbon nitride nanosheets for improving visible-light-driven photocatalytic performance, Adv. Sci. 5 (2018) 1700844, , https://doi.org/10.1002/advs.201700844.

[41] X. Zhang, Z. Meng, D. Rao, Y. Wang, Q. Shi, Y. Liu, H. Wu, K. Deng, H. Liu, R. Lu, Efficient band structure tuning, charge separation, and visible-light response in ZrS$_2$-based Van Der Waals heterostructures, Energy Environ. Sci. 9 (2016) 841–849, https://doi.org/10.1039/C5EE03490F.

[42] F. Yu, Z. Wang, S. Zhang, H. Ye, K. Kong, X. Gong, J. Hua, H. Tian, Molecular engineering of donor–acceptor conjugated Polymer/g-C$_3$N$_4$ heterostructures for significantly enhanced hydrogen evolution under visible-light irradiation, Adv. Funct. Mater. 28 (2018) 1804512, , https://doi.org/10.1002/adfm.201804512.

[43] A. Habibi-Yangjeh, M. Mousavi, Deposition of CuWO$_4$ nanoparticles over g-C$_3$N$_4$/Fe$_3$O$_4$ nanocomposite: novel magnetic photocatalysts with drastically enhanced performance under visible-light, Adv. Powder Technol. 29 (2018) 1379–1392, https://doi.org/10.1016/j.apt.2018.02.034.

[44] S. Asadzadeh-Khaneghah, A. Habibi-Yangjeh, M. Abedi, Decoration of carbon dots and AgCl over g-C$_3$N$_4$ nanosheets: novel photocatalysts with substantially improved activity under visible light, Sep. Purif. Technol. 199 (2018) 64–77, https://doi.org/10.1016/j.seppur.2018.01.023.

[45] A. Habibi-Yangjeh, M. Mousavi, K. Nakata, Boosting visible-light photocatalytic performance of g-C$_3$N$_4$/Fe$_3$O$_4$ anchored with CoMoO$_4$ nanoparticles: novel magnetically recoverable photocatalysts, J. Photochem. Photobiol. A: Chem. 368 (2019) 120–136, https://doi.org/10.1016/j.jphotochem.2018.09.026.

[46] R. Wang, H. Liu, Z. Fan, L. Li, Y. Cai, G. Xu, W. Luo, B. Yang, Y. Zhou, Z. Zou, Unconventional gas-based bottom-up, meter-area-scale fabrication of hydrogen-bond free g-CN nanorod arrays and coupling layers with TiO$_2$ toward high-efficiency photoelectrochemical performance, Nanoscale 10 (2018) 3342–3349, https://doi.org/10.1039/C7NR09244J.

[47] C. Han, Y. Wang, Y. Lei, B. Wang, N. Wu, Q. Shi, Q. Li, In situ synthesis of Graphitic-C$_3$N$_4$ nanosheet hybridized N-doped TiO$_2$ nanofibers for efficient photocatalytic H$_2$ production and degradation, Nano Res. 8 (2015) 1199–1209, https://doi.org/10.1007/s12274-014-0600-2.

[48] S. Zhou, Y. Liu, J. Li, Y. Wang, G. Jiang, Z. Zhao, D. Wang, A. Duan, J. Liu, Y. Wei, Facile in situ synthesis of graphitic carbon nitride (g-C$_3$N$_4$)-N-TiO$_2$ heterojunction as an efficient photocatalyst for the selective photoreduction of CO$_2$ to CO, Appl. Catal. B: Environ. 158-159 (2014) 20–29, https://doi.org/10.1016/j.apcatb.2014.03.037.

[49] V. Kumar, S.Kr. Sharma, T.P. Sharma, V. Singh, Band gap determination in thick films from reflectance measurements, Opt. Mater. 12 (1999) 115–119, https://doi.org/10.1016/S0925-3467(98)00052-4.

[50] J. Ma, X. Tan, T. Yu, X. Li, Fabrication of g-C$_3$N$_4$/TiO$_2$ hierarchical spheres with reactive {001} TiO$_2$ crystal facets and its visible-light photocatalytic activity, Int. J. Hydrogen Energy 41 (2016) 3877–3887, https://doi.org/10.1016/j.ijhydene.2015.12.191.

[51] Y. Zang, L. Li, Y. Xu, Y. Zuo, G. Li, Hybridization of brookite TiO2 with g-C$_3$N$_4$: a visible-light-driven photocatalyst for As^{3+} oxidation, MO degradation and water splitting for hydrogen evolution, J. Mater. Chem. A 2 (2014) 15774–15780, https://doi.org/10.1039/C4TA02082K.

[52] Y. Tan, Z. Shu, J. Zhou, T. Li, W. Wang, Z. Zhao, One-step synthesis of nanostructured g-C$_3$N$_4$/TiO$_2$ composite for highly enhanced visible-light photocatalytic H$_2$ evolution, Appl. Catal. B: Environ. 230 (2018) 260–268, https://doi.org/10.1016/j.apcatb.2018.02.056.

[53] R. Zhong, Z. Zhang, H. Yi, L. Zeng, C. Tang, L. Huang, M. Gu, Covalently bonded 2D/2D O-g-C$_3$N$_4$/TiO$_2$ heterojunction for enhanced visible-light photocatalytic hydrogen evolution, Appl. Catal. B: Environ. 237 (2018) 1130–1138, https://doi.org/10.1016/j.apcatb.2017.12.066.

[54] R. Ye, H. Fang, Y.-Z. Zheng, N. Li, Y. Wang, X. Tao, Fabrication of CoTiO$_3$/g-C$_3$N$_4$ hybrid photocatalysts with enhanced H$_2$ evolution: Z-scheme photocatalytic mechanism insight, ACS Appl. Mater. Interfaces 8 (2016) 13879–13889, https://doi.org/10.1021/acsami.6b01850.

[55] Y. Luo, B. Deng, Y. Pu, A. Liu, J. Wang, K. Ma, F. Gao, B. Gao, W. Zou, L. Dong, Interfacial coupling effects in g-C$_3$N$_4$/SrTiO$_3$ nanocomposites with enhanced H$_2$ evolution under visib light irradiation, Appl. Catal. B: Environ. 247 (2019) 1–9, https://doi.org/10.1016/j.apcatb.2019.01.089.

[56] J. Fu, Q. Xu, J. Low, C. Jiang, J. Yu, Ultrathin 2D/2D WO$_3$/g-C$_3$N$_4$ step-scheme H$_2$-production photocatalyst, Appl. Catal. B: Environ. 243 (2019) 556–565, https://doi.org/10.1016/j.apcatb.2018.11.011.

[57] C. Yang, J. Qin, Z. Xue, M. Ma, X. Zhang, R. Liu, Rational design of carbon-doped TiO$_2$ modified g-C$_3$N$_4$ via in-situ heat treatment for drastically improved photocatalytic hydrogen with excellent photostability, Nano Energy 41 (2017) 1–9, https://doi.org/10.1016/j.nanoen.2017.09.012.

[58] J. Yan, H. Wu, H. Chen, Y. Zhang, F. Zhang, S.F. Liu, Fabrication of TiO$_2$/C$_3$N$_4$ heterostructure for enhanced photocatalytic Z-scheme overall water splitting, Appl. Catal. B: Environ. 191 (2016) 130–137, https://doi.org/10.1016/j.apcatb.2016.03.026.

[59] Z. Jiang, C. Zhu, W. Wan, K. Qian, J. Xie, Constructing graphite-like carbon nitride modified hierarchical yolk–shell TiO$_2$ spheres for water pollution treatment and hydrogen production, J. Mater. Chem. A 4 (2016) 1806–1818, https://doi.org/10.1039/C5TA09919F.

[60] O. Elbanna, M. Fujitsuka, T. Majima, G-C$_3$N$_4$/TiO$_2$ mesocrystals composite for H$_2$ evolution under visible-light irradiation and its charge carrier dynamics, ACS Appl. Mater. Interfaces 9 (2017) 34844–34854, https://doi.org/10.1021/acsami.7b08548.

[61] C. Li, Z. Lou, Y. Yang, Y. Wang, Y. Lu, Z. Ye, L. Zhu, Hollowsphere nanoheterojunction of g-C$_3$N$_4$@TiO$_2$ with high visible light photocatalytic property, Langmuir 35 (2019) 779–786, https://doi.org/10.1021/acs.langmuir.8b03867.

[62] Y. Cao, S. Chen, Q. Luo, H. Yan, Y. Lin, W. Liu, L. Cao, J. Lu, J. Yang, T. Yao, S. Wei, Atomic-level insight into optimizing the hydrogen evolution pathway over a Co$_1$-N$_4$ single-site photocatalyst, Angew. Chem. Int. Ed. 56 (2017) 12191–12196, https://doi.org/10.1002/anie.201706467.

[63] A. Corma, Heterogeneous catalysis: understanding for designing, and designing for applications, Angew. Chem. Int. Ed. 55 (2016) 6112–6113, https://doi.org/10.1002/anie.201601231.